Toward Indoor Simulations of OPV Cells for Visible Light Communication and Energy Harvesting

Daniel Ribeiro Dos Santos, Anne Julien-Vergonjanne, Sadok Ben Dkhil, Marie Parmentier, Pierre Combeau, Stéphanie Sahuguède, Johann Bouclé

To cite this version:

Daniel Ribeiro Dos Santos, Anne Julien-Vergonjanne, Sadok Ben Dkhil, Marie Parmentier, Pierre Combeau, et al.. Toward Indoor Simulations of OPV Cells for Visible Light Communication and Energy Harvesting. IEEE Access, 2024, 12, pp.41027-41041. 10.1109/ACCESS.2024.3378056 . hal-04521240

HAL Id: hal-04521240
https://unilim.hal.science/hal-04521240v1

Submitted on 7 Oct 2024

This article has been accepted for publication in IEEE Access. This is the author's version which has not been fully edited and content may change prior to final publication. Citation information: DOI 10.1109/ACCESS.2024.3378056

Date of publication xxxx 00, 0000, date of current version xxxx 00, 0000.

Digital Object Identifier 10.1109/ACCESS.2022.Doi Number

Towards Indoor Simulations of OPV Cells for Visible Light Communication and Energy Harvesting

Daniel Ribeiro dos Santos[1], Anne Julien-Vergonjanne[1], Sadok Ben Dkhil[2], Marie Parmentier[2], Pierre Combeau[3], Stéphanie Sahuguede[1] and Johann Boucle[1]

[1]XLIM Laboratory, UMR CNRS 7252, University of Limoges, 87032 Limoges, France
[2]Dracula Technologies, 26000 Valence, France
[3]XLIM Laboratory, UMR CNRS 7252, University of Poitiers, 86073 Poitiers, France

Corresponding author: Johann Bouclé (e-mail: johann.boucle@unilim.fr).

This research was funded by the French “Ministère de l’Enseignement Supérieur et de la Recherche” and the IoT-PV Regional project (Région Nouvelle Aquitaine, grant number AAPR2021A- 2020-12033410). The authors are grateful to the CASI board at XLIM for financial support

ABSTRACT The massive deployment of IoT connected devices brings up different modern problems, such as radiofrequency spectrum saturation and energetic requirements. Organic photovoltaics are good candidates for indoor energy harvesting and data reception in a simultaneous lightwave information and power transfer scenario applied for IoT, at which the non-directive channel significantly contributes to the optical system performance. However, achieving the channel impulse response of diffuse links requires complex numerical approaches. This article presents the first ever OPV model used in a Monte-Carlo ray-tracing simulation, associated to theoretical and experimental validation. Finally, for the first time, an optical simulation with an OPV receiver is realized in a cubic environment, from which the received optical power and generated current distributions were obtained. Results show that the employed OPV is suited for indoor energy harvesting to supply low power IoT nodes, and with proper dedicated front-end, could manage to receive optical data in a SLIPT scenario.

INDEX TERMS Channel modelling, experimental demonstration, indoor energy harvesting, optical channel simulation, organic photovoltaics, visible light communication

I. INTRODUCTION

With the expansion of connected objects, the radiofrequency (RF) spectrum is poised to become saturated [1], leading to interest in the terahertz domain and beyond. Wireless communications in the optical domain (optical wireless communication – OWC) have already demonstrated their potential for indoor communication, fulfilling important requirements for some of the internet of things (IoT) demands. By limiting this concept to the visible spectrum, the visible light communication (VLC) technology emerges as a promising technology that takes advantage of indoor lighting for both illumination and data transfer. This was further extended as a network concept in 2011 by Harald Haas, who brought to the spotlight the LiFi term [2], [3], [4], [5].

In classical VLC approaches, a light emitting diode (LED) is used as transmitter, ensuring the conversion of the modulated electrical signal into intensity-modulated (IM) optical waves. Smart lighting systems playing the role of VLC access points have already been deployed and they show great interest for the community in the context of indoor IoT for their reliability and light spectrum recycling [6]. After propagation in free-space, possibly including reflections and transmissions on/through elements of the environment, a photodiode (PD) converts the optical signal into electrical data by generating a current proportional to the received optical power (the so-called direct detection (DD) method) [7]. The received current is generally converted to voltage by a transimpedance amplifier (TIA) [8]. However, this approach requires external power for the current-voltage conversion and to guarantee an ideal operation point of the PD (photoconductive or photovoltaic mode), which represents an important drawback for autonomous systems.

On the energetic side, ambient energy harvesting (EH) is particularly interesting to supply power to connected IoT

This article has been accepted for publication in IEEE Access. This is the author's version which has not been fully edited and content may change prior to final publication. Citation information: DOI 10.1109/ACCESS.2024.3378056

devices, such as sensors and actuators [9]. The innumerous possible usages of these devices in the IoT context, i.e. smart homes, smart cities and smart factories, can easily result in complexity of access for reparation and recharging. From all possible solutions, different EH techniques are available, among which photovoltaic (PV) energy [10], thermal EH [11], RF EH [12] and hybrid configurations [13] stand out. Under indoor situations, obtaining electrical energy from artificial lighting seems promising for the development of autonomous IoT nodes for their high power density, compared to other sustainable sources [14]. Over the past few years, the PV community has displayed significant interest in this area [15], [16], [17], [18], [19].

Today, emerging solar cells (i.e. 3rd generation) are considered as highly relevant PV technologies compared to more conventional inorganic devices (silicon-based systems or thin film technologies), due to their rising performance under full sun and potentially low manufacturing costs and energy payback times [20], [21]. Recent studies have shown the importance of organic photovoltaics (OPVs) for energy harvesting in indoor IoT context [22], [23], [24], [25], [26].

In this context, some studies analyzed the use of PV devices (replacing PDs) as OWC receivers, allowing the simultaneous reception of data (which comes from the AC component of the optical signal) and energy (coming from the DC component) [27], [28], [29], [30], [31], [32], [33], bringing up the simultaneous lightwave information and power transfer (SLIPT) concept. This topology allows the recycling of indoor energy towards autonomous low power IoT nodes while establishing a VLC link through the same optical channel [34]. By selecting an appropriate operating point, the solar cell can provide an acceptable output signal voltage that can be further decoded while still supplying power to the receiver and the involved electronics. Different receiver circuit strategies were also recently developed, aiming the trade-off between energy harvesting and communication performances according to the solar cell operating point [35], [36], [37].

Even though these works validated the performance of solar cells for SLIPT scenarios, they were carried out in line-of-sight (LOS) conditions, obtaining the best data rate and energy harvested when emitter and receiver are aligned, mostly at very short distances (<1 m). No work has analyzed their performance in real and complex indoor IoT scenarios considering all different factors that can impact the receiver capabilities, while only one analyzed the non-line-of-sight (NLOS) contribution on the PV receiver [38]. Actually, signal dispersion due to multipath propagation is generally associated with the reflection of light on different elements of the environment [39]. Consequently, it is important to characterize the optical channel to optimize the performance of the system according to the desired scenario, i.e. to determine the best position and direction of both transmitter and receiver and their ideal optoelectronics features to reach the ultimate communication and EH performance.

In this context, we propose a theoretical and experimental approach to model OPV devices, enabling the evaluation and prediction of EH and communication performance in realistic scenarios based on LOS and NLOS configurations. The established model is used in a Monte Carlo ray tracing (MCRT) software, developed in our laboratory [40], [41], allowing us to obtain the channel impulse response for different optical link configurations. From the simulation results, the received optical power can be computed, which is further extended to illuminance using the luminous efficiency function. From the experimental measurement of the OPV receiver responsivity, which considers different internal parameters of photosensitive devices, the optical power estimation can be converted into short-circuit current, further extended to generated electrical power at maximum power point (MPP) condition.

The experimental validation of our methodology is based on a real OPV device of several cm² (LAYER® technology) inkjet-printed by the French start-up Dracula Technologies (Valence, France). Such tool opens the door to advanced modeling of energy and data link budgets for various devices and nodes of the IoT ecosystem, and for multiple scenarios being targeted by the SLIPT concept. To the best of the authors' knowledge, this is the first OPV modelling used in optical simulation devoted for energy harvesting and communication purposes with experimental validation.

The essential steps required for conducting indoor simulations using the specified OPV are illustrated in Fig. 1, detailed in subsequent sections of the article. Each component is accompanied by its own methodology and corresponding results.

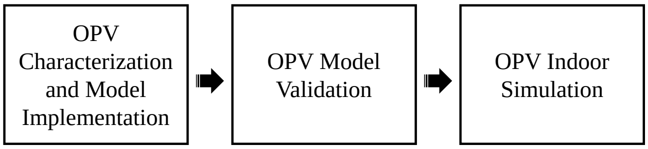

FIGURE 1. Tasks described in each section of the article.

The article is structured as follows: In Section II, we examine pertinent literature, emphasizing the significant contributions of our work to the existing body of knowledge. In Section III, we review the optical channel impulse response equation and describe the responsivity angular dependence of photosensitive devices in general. In Section IV, we detail the materials used for all experiments. Thus, the measurement of the responsivity angular dependence is reported, allowing the implementation of an OPV receiver model into the simulator associated to empirical validation. In Section V, we discuss two experiments, the first consisting in a LOS link and the second in a LOS and NLOS link, experimentally validating the model used for simulations. In Section VI, we simulate a VLC scenario in a 5 m × 5 m × 3 m room, composed by surfaces with spectral reflection coefficients described in [42]. The large spectra simulation provides us the channel impulse response for different positions of the OPV receiver, acquiring then a spatial distribution of the generated current (considered in short circuit conditions), which was then extended to energy harvesting performance under maximum power point operation thanks to previously measuring the current voltage characteristics of the device for different artificial illuminations. Finally, in Section VII, we conclude the work.

II. RELATED WORKS

Indoor environments present unique challenges for EH systems, including limited access to natural sunlight. PV devices offer a viable solution by harnessing ambient light sources such as indoor lighting to generate electrical energy. Furthermore, their communication capabilities have been showcased in the context of VLC, with subsequent expansion into the realm of SLIPT. This section briefly underscores key literature that explores the utilization of PV devices in indoor environments for EH and/or VLC applications.

A. PV DEVICES FOR INDOOR EH

In the present state of IoT, ambient light EH has garnered significant attention across various applications, outlined as follows.

In [43], the authors developed a full autonomous wireless sensor network (WSN) node by employing six commercial flexible PV modules (2.66 cm × 2.075 cm) to monitoring ambient conditions such as temperature, humidity, pressure, acceleration and light intensity. The study simulated an office setting with a consistent 300 lux illumination, finding that the PV panel could generate approximately 275 μW under these conditions. This energy output was deemed sufficient to power other electronic components, including sensors, a microcontroller, and a RF transceiver for data transmission. In [44], the authors employed an oversized OPV module (11 cm × 23 cm) in indoor settings (ranging from 400 lux to 1000 lux) over a period of 21 months. While the actual generated power remains undisclosed, the OPV effectively powered all other electronic components with the assistance of a battery. Yet, the precise OPV dimensions needed to power the setup, factoring in the final system size, remain uncertain. In [45], the authors developed a full autonomous indoor WSN by employing a 5.81 cm × 4.86 cm amorphous silicon (α-Si) PV cell, considering a constant 200 lux illumination (generating around 137.1 μW) to design the circuit. Finally, Meli et al. developed an autonomous sensor node operating at incredibly low illuminances (5 lux) [46]. The system, associated to energy management strategies, supplied a touch detector, a real-time clock and a microcontroller with four 98 mm² PV cells.

Expanding the application of indoor PV EH to the medical field, Tran et al. developed a highly efficient IoT node for medical surveillance employing a large and flexible amorphous silicon thin-film solar panel measuring 19 cm × 4 cm in dimensions [47]. Despite the architecture's inability to directly charge the battery, it still enhances its longevity under indoor conditions (irradiances lower than 3 mW/cm²). This underscores the significance of the current strategy.

B. PV DEVICES FOR SLIPT

By employing a PV cell/module in an environment featuring VLC, the IoT node not only harvests energy from indoor ambient light but also detects its intensity to decode optical data. With a customized front-end circuit, the receiver can distinguish between data and energy. While the previous section showcased intriguing real-world indoor lighting EH for IoT systems, the SLIPT concept is relatively novel, and no study has yet presented a fully autonomous and operational system under practical indoor conditions. We then briefly highlight some significant findings regarding indoor SLIPT.

In [48], the first full autonomous IoT node was developed using light for both communication and energy transmission, but it only worked within a short distance of 1 m between the light source and the receiver. A 11 cm × 16.5 cm silicon (Si) PV module was used to power the entire node with a corresponding irradiance of 5 mW/cm², achieving around 4.8 kbit/s. In [49], a 9.36 cm² α-Si module was used to receive a 2.6 kbit/s error free data at 1 m distance. Carrascal et Al. considered a constant 200 lux illumination to estimate the PV device EH performance, obtaining a maximum of 96.9 μW output power.

Hammoud et al. theoretically simulated the optical channel in a 3 m × 3 m × 3 m empty room with two optical sources, focusing on the SLIPT context [50]. Their study was purely theoretical, involving only LOS simulations, and assumed a constant power conversion efficiency (PCE) of 18%.

Other contributions to the field focus on characterizing the performance of PV devices in energy harvesting and communication, but they do not take into account real-life complex IoT environments as most are realized under LOS configuration. For those interested in delving deeper into the topic, we suggest the following reference for a better understanding [51].

C. OUR CONTRIBUTION

As detailed in Section II.A, the applicability of PV devices for indoor EH is large. However, most works estimate a constant illumination to simulate indoor situation, being able to model the best EH architecture for the proposed scenario. Moreover, other studies utilized autonomous systems in undisclosed indoor settings, effectively monitoring the surroundings but lacking any forecast of the energy harvesting potential before the measurements. Additionally, actual experimental studies on SLIPT do not encompass scenarios beyond LOS conditions. In [50], a simulation (also in LOS link) was realized, but without any experimental validation of the proposed approach.

Ultimately, in our work, we experimentally validate the simulation of an OPV considering both LOS and NLOS links. This capability enables us to simulate the device across

This article has been accepted for publication in IEEE Access. This is the author's version which has not been fully edited and content may change prior to final publication. Citation information: DOI 10.1109/ACCESS.2024.3378056

various indoor scenarios, allowing a short-circuit current estimation (extended to generated power), contributing to the current state-of-the-art for both indoor EH and SLIPT in the following ways:

1) By analysing the power distribution across an indoor IoT environment, we can optimize the placement and orientation of WSN nodes to suit specific applications, while also refining EH systems and techniques;
2) In the context of SLIPT, we employ the same strategy outlined in point 1), while considering the maximum bandwidth constrained by the optical channel. This allows for the optimization of the receiver system to fulfill specific quality of service requirements;
3) The simulations can be readily extended to IoT scenarios involving mobility, addressing both energy harvesting and communication aspects.

III. OPTICAL PROPAGATION AND OPV CHARACTERISTICS

In this section, a review of the optical channel impulse response is realized, highlighting some important parameters in optical communications, as well as the wavelength dependence of non-directive paths. The angular dependence of the receiver responsivity $R(\lambda, \Psi)$, a parameter that indicates the ratio between the short-circuit current and the incident optical power, is also described.

We consider that no concentrator or optical filter is employed at the reception and that the source is punctual and follows a Lambertian radiation pattern with directivity m_1 [52]. The radiant intensity I of Lambertian sources follows a cosine power behavior, as shown in (1), where I_0 is the maximum irradiance (obtained at normal radiation) and θ is the angle of radiance (equivalent to elevation angle in polar coordinates) [7]:

$$I(\theta) = I_0 \cos^{m_1}(\theta) \tag{1}$$

The directivity m_1 characterizes the ability of the Lambertian source to focus the optical power P_t in a specific direction. This attribute is directly correlated with the half-power angle $\theta_{1/2}$, which identifies the angle at which the radiant intensity I equals half of its peak value I_0. The relation between both variables can be seen in (2) [7].

$$m_1 = -\frac{\ln(2)}{\ln(\cos\theta_{1/2})} \tag{2}$$

Equation (2) illustrates that sources with higher directivity m_1 concentrate more optical power per steradian, resulting in a decrease in $\theta_{1/2}$.

A. CHANNEL CHARACTERISTICS

The channel impulse response describes how the channel responds to an impulse (or Dirac $\delta(.)$) optical input, in function of the time t, and depends on the direct and diffuse paths followed by the optical signal. In wide spectrum communications, it also has a strong wavelength dependence due to the spectral reflectivity of surfaces that induce non-direct rays [42]. However, the channel impulse response depends on each wavelength λ independently, and is then noted as $h(t;\lambda)$. For multiple sources, it can be expressed as shown in (3) [42].

$$h(t;\lambda) = \sum_{n=1}^{N}\left(h_n^{(0)}(t) + \sum_{k=1}^{\infty} h_n^{(k)}(t;\lambda)\right) \tag{3}$$

where k represents the number of light reflections before achieving the receiver and N is the number of sources in the link. Thus, $h_n^{(0)}(t)$ corresponds to LOS contributions and $h_n^{(k)}$ corresponds to the NLOS ones. The channel behavior is analyzed by determining different characteristics obtained from $h(t;\lambda)$, such as the static gain (channel DC gain) and the delays leading to temporal dispersion of the channel. For most analysis, we consider only one source for the optical link without loss of generality. In the end of the current section, the review is then brought to a multiple source scenario.

The ratio between the average transmitted optical power P_t, emitted by the source, and received optical power P_r that arrives at the photoreceiver active surface A_r, i.e. the surface that absorbs the photons, is described by the channel DC gain H_0, which can be split into two different components, LOS (H_{LOS}) and NLOS (H_{NLOS}), and is defined as follow [7]:

$$H_0 = H_{LOS} + H_{NLOS} = \frac{P_r}{P_t} \tag{4}$$

In LOS paths, the impulse response $h^{(0)}(t)$ has no actual wavelength dependence (for indoor scenarios) and is described by a time-shifted impulse function with amplitude H_{LOS}, as shown in (5), where d is the distance between emitter and receiver and c is the speed of the light in vacuum . This equation considers that the incidence angle Ψ on the receiver surface and that the radiance angle θ are both inferior to 90° [7].

$$h^{(0)}(t) = h_{LOS}(t) = H_{LOS}\delta\left(t - \frac{d}{c}\right) \tag{5}$$

In LOS links, the channel DC gain H_{LOS} is obtained by integrating the impulse response $h^{(0)}(t)$ over the specified time period. For NLOS links, the same principle applies, but the integration needs to be performed separately for each individual wavelength.

By considering that the solid angle subtended by the active surface A_r and the punctual source is infinitesimal (which can be considered as valid for many real cases in a first approximation, where $d \gg A_r$), H_{LOS} can be analytically obtained as follow [7]:

This article has been accepted for publication in IEEE Access. This is the author's version which has not been fully edited and content may change prior to final publication. Citation information: DOI 10.1109/ACCESS.2024.3378056

$$H_{LOS} = A_r \frac{m_1 + 1}{2\pi d^2} \cos^{m_1}(\theta) \cos(\Psi) \tag{6}$$

In LOS only scenarios, the knowledge of the source optical power P_t allows to determine the power that arrives at the receiver P_r using (6) and (4). However, in complex situations where NLOS rays play an important role in the total power collected by the receiver, multiple reflections on different surfaces must be considered. The channel impulse response for a finite number of reflections has to be computed, which can easily increase the complexity by considering high reflection orders and multiple wavelengths (like for white LED).

Thus, the received power spectral distribution (PSD) $\Phi_r(\lambda)$ is related to the PSD of the source $\Phi_t(\lambda)$ by (7) [53], where the integral represents the channel DC gain as a function of the wavelength. The total received optical power considering the band of interest (for VLC, the whole visible band) is described by (8) [54].

$$\Phi_r(\lambda) = \Phi_t(\lambda) \int_{-\infty}^{\infty} h(t;\lambda) dt \tag{7}$$

$$P_r = \int_{\lambda} \Phi_r(\lambda) d\lambda = \int_{-\infty}^{\infty} \int_{\lambda} \Phi_t(\lambda) h(t;\lambda) d\lambda dt \tag{8}$$

The PSD $\Phi_t(\lambda)$ can be obtained according to its normalized emitted power $S(\lambda)$ (note that $\int S(\lambda) d\lambda = 1$) as shown in (9), which results in P_r described by (10).

$$\Phi_t(\lambda) = P_t S(\lambda) \tag{9}$$

$$P_r = P_t \int_{-\infty}^{\infty} \int_{\lambda} S(\lambda) h(t;\lambda) d\lambda dt \tag{10}$$

We define then in (11) $h_\lambda(t)$ as the channel impulse response pondered by the normalized PSD of the source $S(\lambda)$, resulting in the received optical power P_r defined by (12).

$$h_\lambda(t) = \int_{\lambda} S(\lambda) h(t;\lambda) d\lambda \tag{11}$$

$$P_r = P_t \int_{-\infty}^{\infty} h_\lambda(t) dt \tag{12}$$

The channel DC gain H_0 in wide spectrum links is then obtained by (13).

$$H_0 = \int_{-\infty}^{\infty} h_\lambda(t) dt \tag{13}$$

Although diffuse channels provide good reliability for systems susceptible to blockage, they can be time dispersive. The channel impulse response pondered by the source normalized PSD $h_\lambda(t)$ can provide some important parameters of multipath channels, for instance the mean delay spread μ and root mean square delay spread D_{rms} of the configuration, defined by (14) and (15) respectively [53].

$$\mu = \frac{\int t h_\lambda^2(t) dt}{\int h_\lambda^2(t) dt} \tag{14}$$

$$D_{rms} = \left[\frac{\int (t-\mu)^2 h_\lambda^2(t) dt}{\int h_\lambda^2(t) dt} \right]^{1/2} \tag{15}$$

Approaches based on MCRT allow the evaluation of the impulse response $h(t;\lambda)$ for multiple independent wavelengths and multiple sources in cases of complex scenarios, even considering a large number of reflections. For configurations with N sources, the received optical power P_r can be obtained for each source independently, as defined by (16) [42].

$$P_r = \sum_{n=1}^{N} P_{t_n} \int_{-\infty}^{\infty} h_{\lambda_n}(t)\, dt \tag{16}$$

Finally, for identical optical sources (in both normalized PSD $S(\lambda)$ and transmitted power), the total received optical power is:

$$P_r = P_t \int_{-\infty}^{\infty} \int_{\lambda} S(\lambda) \sum_{n=1}^{N} h_n(t;\lambda)\, d\lambda dt \tag{17}$$

Beyond the optical channel, systems based on photodetectors convert the received optical power P_r into electric power. Thus, some of the most important photosensitive devices characterizations are realized under short-circuit conditions, described in the next section for an OPV.

B. OPV SHORT CIRCUIT CURRENT I_{SC}

For the analysis presented in this article, the authors exploited the single-diode model for the OPV electrical representation (see Fig. 2), a first level approximation that is well accepted by the community for its performance accuracy in static operations [55].

The model describes the solar cell internal electrical properties, such as voltage drop and recombination losses. Multiple load values R_L result in different obtainable output current I_{out} and output voltage V_{out}, going from the short-circuit condition, at which the current is at its maximum I_{sc}, up to the open circuit condition, at which the voltage is at its maximum V_{oc}. Changing the operation point of the OPV results in different static and dynamic performances. To obtain

This article has been accepted for publication in IEEE Access. This is the author's version which has not been fully edited and
content may change prior to final publication. Citation information: DOI 10.1109/ACCESS.2024.3378056

the actual generated current I_{ph} we require knowledge of all internal parameters of the device (D, R_{sh}, R_s), which is further achievable with $I(V)$ curves measurements, a static characterization well known by the photovoltaic community.

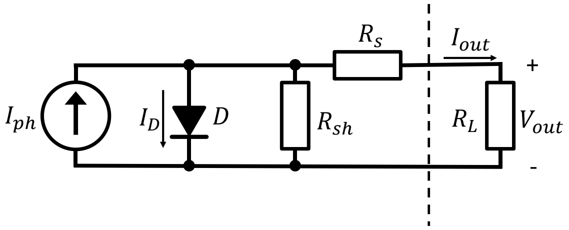

FIGURE 2. **OPV single diode electrical model with load R_L.**

The responsivity describes the device's capability to convert optical power into short-circuit current I_{sc}, while also accounting for the internal losses of the device. Different factors can influence the device's responsivity, including the materials used in each layer of the structure, their energy band gaps, incident light wavelength and the angle of incidence, affecting photon-electron interaction cross-sections and potential reflections due to layer stacking. For each experiment described in next sections, the OPV operates in short circuit condition and only the I_{sc} is measured, without any specific extraction of the actual generated current I_{ph}.

With the responsivity $R(\lambda)$ (which is found in most commercial photodetectors datasheets), we can extend the MCRT analysis to obtain the short-circuit current from the received power in a desired simulation scenario. However, this parameter has an angular dependence, which is described in the next section.

C. RELATIVE RESPONSIVITY $R_{rel}(\Psi)$

The angular dependence of the responsivity of photosensitive devices, i.e. the ability to generate current as a function of the angle of incidence Ψ of the optical power for a given wavelength, is important for systems modelling and performance predictions. In the most general case, the real responsivity $R_{real}(\lambda, \Psi)$ depends on both wavelength λ and incident angle Ψ simultaneously, and as a matter of fact, these variables are not independent, which means that different Ψ can result in different spectral responsivity $R(\lambda)$ [56], [57]. Since the short-circuit current depends on angular factors, it is mostly impossible to analytically compute it in complex scenarios, and simulation tools have to be used. However, the full implementation of $R_{real}(\lambda, \Psi)$ inside a simulator is not trivial, so, in a first approach, let us consider that λ and Ψ are independent variables so that the responsivity can then be expressed as follow [56]:

$$R_{real}(\lambda, \Psi) = R(\lambda) R_{rel}(\Psi) \tag{18}$$

where $R_{rel}(\Psi)$ is the relative responsivity, a normalized function that defines the global behavior of the photosensitive device according to the incident angle. The independent variables hypothesis is actually valid for low variations of the responsivity spectra according to the incident angle [58]. The short-circuit current I_{sc} angular dependence can be explicitly seen in (19) [7]:

$$\begin{gathered} I_{sc}(\Psi) = \int_{\lambda} R_{real}(\lambda, \Psi) \Phi_r(\lambda) d\lambda \\ I_{sc}(\Psi) = R_{rel}(\Psi) \int_{\lambda} R(\lambda) \Phi_r(\lambda) d\lambda \end{gathered} \tag{19}$$

The incidence angle dependence can be seen in both received optical power P_r, following a $\cos(\Psi)$ pattern in LOS (seen in (6)) and NLOS links, and short-circuit current I_{sc}, following an arbitrary function $R_{rel}(\Psi)$. However, these two dependences are necessarily linked in a way that I_{sc} rely on the received optical power (and therefore on $\cos(\Psi)$) and on the conversion capability $(R_{rel}(\Psi))$.

Thus, similar to the source, the photoreceiver can also describe different angular behavior for the generated current, defined by the function $R_{rel}(\Psi)\cos(\Psi)$. Some devices manifest Lambertian responses, at which the short-circuit current follows a cosine power expression with associated half-current angle $\Psi_{1/2}$ (please note that the term half-power angle is inaccurate, since $R_{rel}(\Psi)$ describes the conversion capability of the device), which can also be associated to the receiver directivity. Although $R_{rel}(\Psi)\cos(\Psi)$ can be easily found in Si-based commercial photodiodes datasheets, it is an unknown parameter for most photovoltaic devices, including thin film OPVs. We therefore perform its experimental characterization in Section IV. Finally, Fig. 3 shows a simple diagram that contains all main variables that are analyzed in the current work.

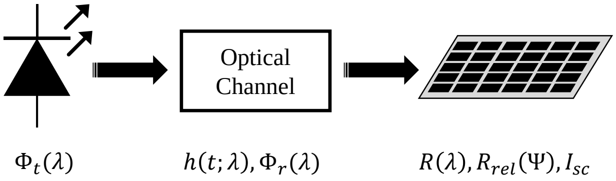

FIGURE 3. **Diagram containing all variables analyzed in the current work.**

IV. OPV ANGULAR CHARACTERIZATION

In this section, we describe the materials used for all experimental work, the methodology to characterize $R_{rel}(\Psi)\cos(\Psi)$ and the obtained results.

A.MATERIALS

In subsequent sections, all experimental work is realized with the same material. A single OPV cell provided by Dracula Technologies and based on their LAYER® technology was used as photoreceiver, and an OSRAM LE CW E3B high power white LED was used as optical source. Fig. 4 shows the

This article has been accepted for publication in IEEE Access. This is the author's version which has not been fully edited and content may change prior to final publication. Citation information: DOI 10.1109/ACCESS.2024.3378056

OPV device, with 4.7 cm length and 0.66 cm width, fabricated on a flexible substrate using entirely inkjet printing technique.

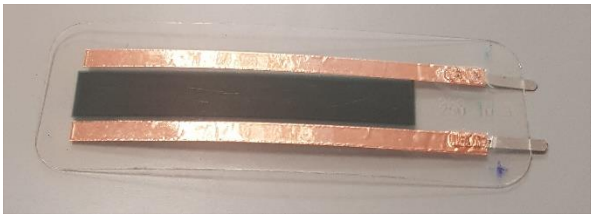

FIGURE 4. **OPV based on LAYER® technology. Fabricated by Dracula Technologies.**

The LED source has a 65° half-power angle $\theta_{1/2}$, which corresponds to a directivity m_1 of 0.8048. Its normalized emitted power was measured using BLACK-Comet, a dedicated spectrometer developed by StellarNet Inc, and is shown in Fig. 5. Thus, the OPV spectral responsivity $R(\lambda)$ (equally shown in Fig. 5) was obtained by external quantum efficiency characterization (no-bias, DC mode) with the QE-T system, developed by Enlitech.

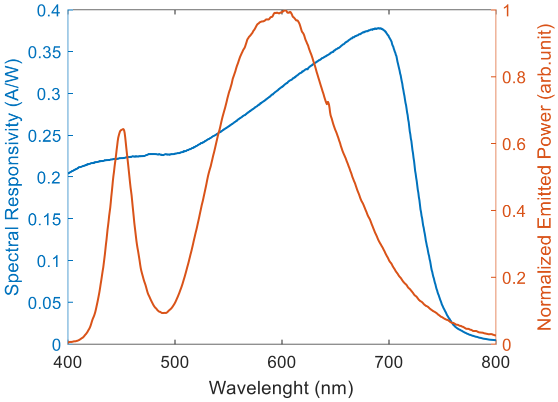

FIGURE 5. **OPV spectral responsivity R(λ) (in blue) and normalized emitted power (in red).**

The characterization and OPV model validation (Sections IV and V respectively) are based on the short-circuit I_{sc} current measurement, realized with a Keithley 2621B source-measure unit.

For each experiment, we employed a meticulously constructed bench, developed in XLIM laboratory (refer to Fig. 6). This setup, initially devised to establish a LOS link, facilitates adjustments to the receiver incident angle Ψ while preserving the source-receiver distance and source orientation constant. To avoid any undesired reflected rays or ambient noise, all the structure is painted with high absorbing black mate ink and measurements are realized under dark conditions. This experimental bench can be adjusted to include NLOS link by including reflective surfaces by the receiver (used in Section V.B for NLOS validation). To measure the spectral reflectance of these surfaces, a dedicated spectrophotometer (Agilent Cary 300) was employed.

Further OPV characterizations are described in supporting information. Its $I(V)$ curve under 1000 lux (realized with a Dalle LED Philips 60x60cm, 4385K) is shown Supp. Fig. 1, which presents an open-circuit voltage of 0.64 V and 306 μA short-circuit current. Its $P(V)$ characterization under the same condition is also shown in supporting information, Supp. Fig. 2, obtaining a maximum output power of 137 μW at maximum power point (0.525V).

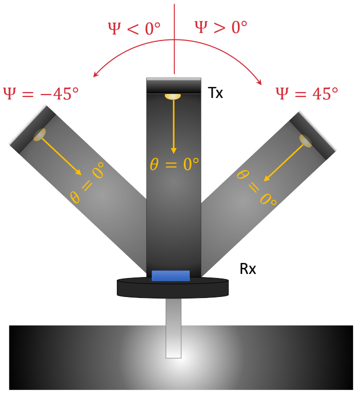

FIGURE 6. **Experimental bench used in each experiment.**

B. METHODOLOGY

As detailed in Section III, it is not possible to analytically obtain the optical power that arrives on a photoreceiver (and by consequence the short-circuit current) in NLOS links. Therefore, to obtain the $R_{rel}(\Psi)$ function, we must rely upon the LOS equation described in (6). With (19), (7), (5) and (6), the short-circuit current of a receiver in a LOS configuration can be mathematically described as follows:

$$I_{sc}(\Psi) = A_r\left(\frac{m_1+1}{2\pi d^2}\right)\cos^{m_1}(\theta)\cos(\Psi)\,R_{rel}(\Psi)\int_{\lambda} R(\lambda)\Phi_t(\lambda)d\lambda \tag{20}$$

By fixing the distance d, keeping the source always pointing towards the receiver ($\theta = 0°$) and changing the angle of incidence, the current varies according to Ψ and can be measured, obtaining then the angular dependence of the current $I_{sc}(\Psi)$. In this way, the terms that do not depend on the incident angle are constant and the $R_{rel}(\Psi)\cos(\Psi)$ function can be obtained. However, experiments are susceptible to errors, which would directly affect $R_{rel}(\Psi)$, a function that is intrinsically normalized. It can then be obtained by (21), where I_{SCmax} is the maximum value of the measured current, normally obtained in direct LOS configuration ($\theta = 0°$ and $\Psi = 0°$).

$$R_{rel}(\Psi)\cos(\Psi) = \frac{I_{sc}(\Psi)}{I_{SCmax}} \tag{21}$$

C. $R_{rel}(\Psi)$ MEASUREMENT

For the measurement, a LOS link was employed while fixing the distance $d = 25.1$ cm and the angle of irradiance $\theta = 0°$, with means of the developed bench (see Fig. 6).

Because $R_{rel}(\Psi)\cos(\Psi)$ is normalized, the real value of the transmitted optical power P_t is not relevant, but the stabilization of the emitting LED is crucial over the experiment. For better robustness, the characterization is realized for negative and positive values of Ψ in order to verify any deviation of the OPV response from the expected polar symmetry in such LOS configuration. We also note that this angular characterization can depend on the selected horizontal orientation of the OPV device on the test bench.

D. CHARACTERIZATION RESULTS

Fig. 7 shows the $R_{rel}(\Psi)\cos(\Psi)$ measured from the OPV, which almost perfectly fits a Lambertian pattern presenting a half-current angle $\Psi_{1/2}$ of 60°, resulting in a unitary directivity. In fact, this demonstrates that this particular OPV responsivity has no specific angular dependence, as $R_{rel}(\Psi) = 1$. Interestingly, we note that this is the most common behavior of commercial Si-based photodiodes (fact that can be verified in most datasheets), consequently, a photodiode simulation model can be employed for indoor MCRT simulation for this particular OPV cell. This fact was not a priori so obvious considering that OPV cells are based on a stack of materials of thickness in the order of visible wavelengths. For the given distance, a perfect azimuth symmetry was observed with aid of multiple experiments, as consequence, the short-circuit current depends only on the polar angle, which is expressed by the incident angle Ψ dependence.

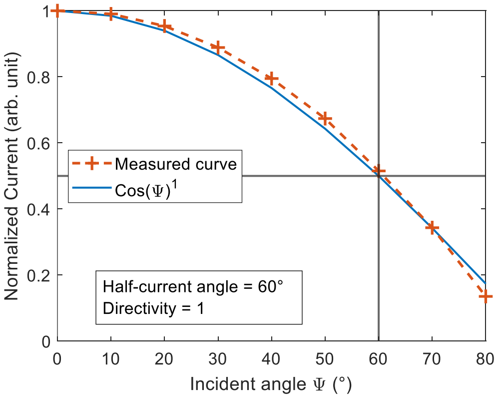

FIGURE 7. **Measured $R_{rel}(\Psi)cos(\Psi)$ (in red) and theoretical Lambertian receiver with 60° half-current angle (in blue).**

Knowing that the simulator is already designed to operate with different Lambertian receivers, the OPV device was then implemented by accounting for its rectangular dimensions (4.7 cm and 0.66 cm) and experimental $R_{rel}(\Psi)\cos(\Psi)$ with half-current angle of 60°.

V. OPV MODEL VALIDATION

A. METHODOLOGY

To validate the simulation results using the OPV receiver, two different experiments were realized, the first based on a LOS link, and the second based on a LOS and NLOS link.

The simulator can provide the impulse response $h(t;\lambda)$ in any modelled configuration, being then extended to the received PSD $\Phi_r(\lambda)$ with (7). For 60° half-current Lambertian receivers, $R_{rel}(\Psi) = 1$, consequently I_{sc} can be directly obtained from (19), (7) and (9), as follows:

$$I_{sc} = P_t \int_{-\infty}^{\infty} \int_{\lambda} R(\lambda)S(\lambda)h(t;\lambda)d\lambda\, dt \qquad (22)$$

Considering the angular characterization of the device presented in the previous section, the photodiode model is hence directly applicable to the OPV cell provided by Dracula Technologies. In the following parts, the simulations are therefore confronted to experimental measurements made using our characterization bench described in Section IV.A. Fig. 8 depicts the methodology employed to validate the OPV model through MCRT simulation.

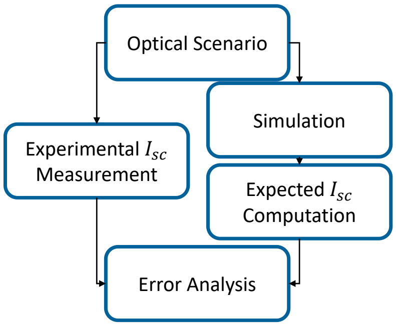

FIGURE 8. **Flowchart of employed methodology for the OPV model validation employing MCRT simulations.**

Among the different sources of errors arising between our simulated and experimental currents, the accuracy of the LED emitter calibration (its normalized PSD and P_t) is the most important factor. Therefore, a (pessimistic) $\pm 5\%$ error bar is systematically considered on the experimental current to account for these uncertainties.

To determine the simulated current, it is necessary to know the value of the emitted PSD $\Phi_t(\lambda)$. To this end, we used the BLACK-Comet spectrometer in a perfect alignment configuration ($\Psi = 0°$ and $\theta = 0°$) to measure the received power at the given distance d and so to obtain the corresponding emitted power using (6).

A. LOS LINK

1. SCENARIO DESCRIPTION

Dracula Technology's OPV was placed in the configuration shown in Fig. 6, with its length aligned to the bench rotation axis. With the distance $d = 15.4$ cm, the short-circuit I_{sc} was

This article has been accepted for publication in IEEE Access. This is the author's version which has not been fully edited and
content may change prior to final publication. Citation information: DOI 10.1109/ACCESS.2024.3378056

measured for different incident angles and was compared to the simulated current.

In fact, for LOS links, a ray propagation software is not necessary, as the channel DC gain can be described by the analytical expression (6), has no wavelength dependence and can be easily calculated. We also aim to compare the experiment and simulation with the theoretical short circuit current, derived from (6) and (22).

2. RESULTS

Finally, Fig. 9 shows the obtained theoretical (in blue), simulated (in yellow), and experimental (in red) short-circuit currents I_{sc} for multiple incident angles Ψ.

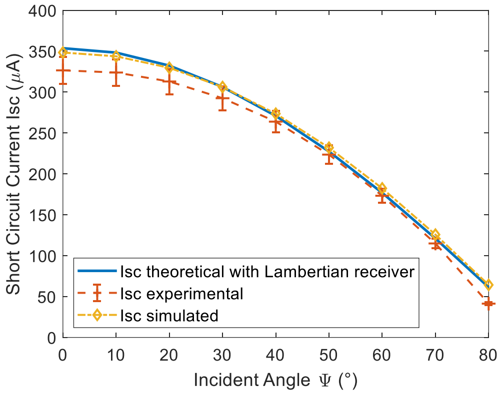

FIGURE 9. **Theoretical generated current using LOS link equation (23) (in blue), experimental current (in red) with 5% error bar and current obtained from simulation results (in yellow).**

We notice that the experimental results are very close to the simulated ones and follow the theoretical behavior, within the accuracy of our experimental measurements. This LOS result is a preliminary validation of the OPV model, which allows an accurate prediction of the current generated by the photovoltaic device in LOS scenarios. In Section V.B, a hybrid scenario consisting of LOS and NLOS contributions is simulated and validated through experimentation.

B. LOS + NLOS LINK

1. SCENARIO DESCRIPTION

The experimental validation of the OPV model in LOS + NLOS link is essential for future simulations in complex situations, especially for indoor IoT applications. In this context, for increased accuracy, the reflected light component H_{NLOS} must approach or surpass H_{LOS}, denoting that materials with high reflectance in the visible spectrum must be pondered. In Section V.A, the simulation did not contemplate any particular wavelength analysis as the LOS channel attenuation is constant for all optical spectrum. However, materials have different reflectances for different wavelengths, which must be accounted for precise prediction of the short-circuit current provided by the OPV receiver.

Reflection surfaces are made of materials which reflect the light in different ways, modeled by the bidirectional reflectance distribution function (BRDF) [59]. Some of them are perfectly diffuse (Lambertian BRDF), other ones are perfectly specular (dielectric BRDF), and the rest, i.e. most of them in fact, are part diffuse and part directive (Blinn-Phong BRDF for instance). Although most materials that compose indoor complex scenarios are often considered as Lambertian, these three BRDF are implemented in the simulator.

Our characterization bench was then adapted to include NLOS contributions in the experiment. Two metal plates were placed at 10 cm from the center of the structure, where the OPV is hold (with its length in the same axis as the rotation bench), and to avoid any specular reflections, both walls were covered with white paper, a mostly diffuse material with spectral reflectance $\rho_{paper}(\lambda)$ that follows a Lambertian pattern.

The spectral reflectance $\rho_{paper}(\lambda)$ was measured under normal incidence. The obtained measurements as well as the source normalized emitted power can be seen in Fig. 10.

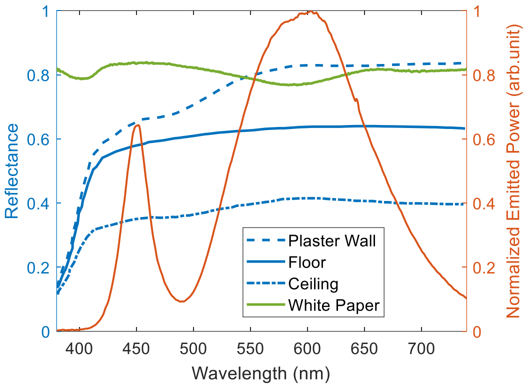

FIGURE 10. **Spectral reflectance of white paper (used in Section V), of the materials that compose the room [42] for the simulation (used in Section VI) and the normalized emitted power of the source.**

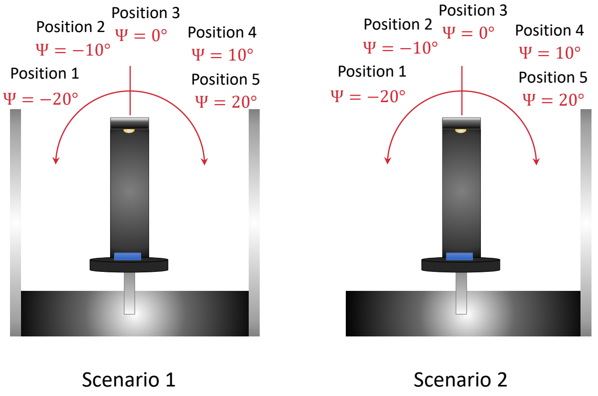

FIGURE 11. **Scenarios for NLOS experiment.**

Interestingly, the reflectance is almost constant over the entire visible spectrum at around 0.8. As detailed in Section III, large spectra diffuse simulations require more

This article has been accepted for publication in IEEE Access. This is the author's version which has not been fully edited and content may change prior to final publication. Citation information: DOI 10.1109/ACCESS.2024.3378056

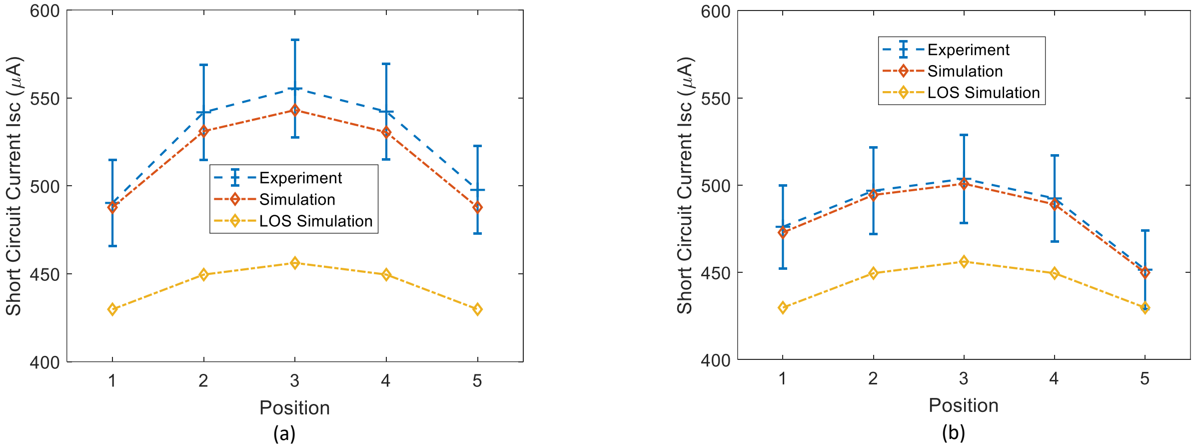

(a)

(b)

FIGURE 12. Measured current in NLOS scenario with 5% measurement error (in blue) with associated expected current obtained with simulation (in red) and LOS component obtained with simulation (in yellow). (a): Scenario 1; (b): Scenario 2.

processing time than narrowband spectra ones due to the spectral reflectance $\rho(\lambda)$ of surfaces that compose the environment. As each wavelength can be analyzed separately, we can then perform multiple simulations for different λ. After obtaining all results considering the total spectra of interest, the channel impulse response $h(t;\lambda)$ is obtained, which can be extended to short circuit results with (22).

The spectrum of interest goes from 380 nm up to 740 nm. It was then discretized with a 10 nm step and a single-input-single-output simulation was realized for each wavelength. Two different scenarios were analyzed: the first containing both paper walls and the second with only one paper wall on the right side. For each situation, five incident angles Ψ were chosen, from -20° to 20° with a 10° step (see Fig. 11).

In the literature, it has been demonstrated that considering 3 reflections in a Monte-Carlo based simulations in conventional indoor scenarios is sufficient to well estimate the channel [60]. However, in the current situation, the distances between Tx, Rx and the walls are in the order of centimeters, increasing the reflection dependence of the system. Thus, in our configuration, we have to consider ten reflections, according to one million rays with ray-gathering simulation algorithm [40] to provide both realistic and sufficiently converged impulse response $h(t;\lambda)$. We also kept the $\pm 5\%$ error bars on the experimental current to account for our experimental accuracy. Aiming to experimentally verify the reflected rays influence on the system, the LOS channel contribution is also simulated.

2. RESULTS

First, we remark from Fig. 12 that for both scenarios, the measured and simulated results are very close, which shows the validity of the model implemented for the OPV cell in the MCRT simulator while accounting LOS and NLOS rays. Fig. 12 also confirms the impact of the reflected rays, increasing the short circuit current by 21% for the first scenario (at which the NLOS component is more significant) and by 10% for the second one.

In the case of scenario 2 where the left wall is removed, the total gain decreases and approaches the value corresponding to a LOS link, as shown in Fig. 12 (b).

We emphasize that the real current generated by OPV devices is governed by the cell's behavior (parasitic resistances, ideality factor, etc.). In short-circuit conditions, our methodology enables the prediction of short-circuit current with a good accuracy. These predictions can easily be extended to the generated power P_{out} under various load conditions through the preliminary knowledge of the cell's electrical characteristics under different illuminations, obtained through conventional $I(V)$ curves measurements. In Section VI, we explore, for the first time, a realistic simulation under indoor conditions, from which we are able to predict the power harvested by an OPV receiver exposed to multiple LED sources.

VI. INDOOR SIMULATION

For simplicity, we chose the same scene described in [42] for the OPV simulation, with the same spectral reflectance but different source PSD. The spectral reflectance of materials that compose the environment and the source normalized emitted power are shown in Fig. 10. Contrary to our NLOS experiment, all materials have reflectance that deeply depends on the wavelength. For the simulation, four LEDs with half-power angle of 60° were fixed at the ceiling facing downward, and the OPV was placed 10 cm above the ground facing upward. The rectangular OPV cell was then considered at 400 different positions in the X and Y axis, with its length aligned to the X axis, allowing to precisely map the received optical power P_r (and consequently the short-circuit current I_{sc}) for each placement. Thirty-seven different wavelengths were used for the simulation, going from 380 nm up to 740 nm with 10 nm step, providing a good trade-off between precision and processing time. A convergence analysis was carried on, showing that 5 million rays with ray-gathering algorithm provided good accuracy for the simulation. Table 1 shows some of the simulation parameters.

TABLE 1
SIMULATION PARAMETERS

LED 1 position	(1.5, 1.5, 2.99)
LED 2 position	(1.5, 3.5, 2.99)
LED 3 position	(3.5, 1.5, 2.99)
LED 4 position	(3.5, 3.5, 2.99)
LED optical power	4 × 1 W
Number of rays	5 million
Maximum considered reflections	3
Time step Δt	0.15 ns
Total time length	120 ns

With the channel impulse response $h(t;\lambda)$ (that for N sources is the sum of each $h_n(t;\lambda)$, as shown in (3)) obtained through simulation at each position, $h_\lambda(t)$ could be computed with (11).

1. RESULTS AND DISCUSSIONS

Fig. 13 shows the pondered channel impulse response obtained in two positions: the first in the centre (in blue), where most contributions arise from the LOS channel; and the second in the corner (in red), from which we highlight the multipath channel due to different peaks in different time values.

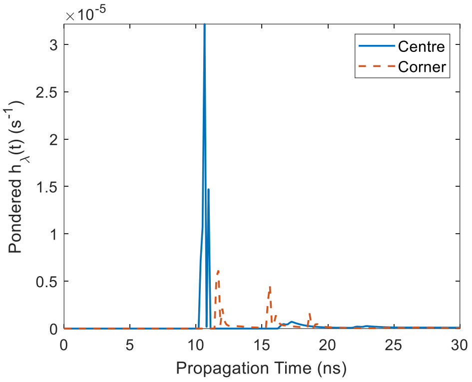

FIGURE 13. Simulated $h_\lambda(t)$ at the centre (in blue) and at the corner (in red).

The spectral reflectance of each surface that composes the environment has major importance on the received power spectra $\Phi_r(\lambda)$. As the receiver approaches the corners of the scene, the NLOS component significantly increases, being then in the same order of magnitude to the LOS one. An interesting attenuation of lower wavelengths was observed at different positions in the environment by comparing the normalized received PSD to the normalized emitted PSD, demonstrating the reflectance influence on the wide spectrum link.

From $h_\lambda(t)$, the delay spread could be computed with (14) and (15), obtaining 1.13 ns at the centre, increasing up to 3 ns at the corner. For communications with negligible inter-symbol interference (ISI), the maximum channel bandwidth $B_{channel}$ is limited to $B_{channel} \leq \frac{1}{10 \times D_{rms}}$ [61], [62], resulting in 89 MHz and 33 MHz at the centre and corner respectively. In fact, large area photodetectors, such as the current OPV, are associated with large geometric capacitance, which limits their response time, considering a classical first-order low pass filter behaviour, that will decrease the system bandwidth. In consequence, the maximum achievable data rate in the simulated scenario is expected to be limited by the OPV itself, not by the channel multipath characteristics.

Dividing the received optical power spectra $\Phi_r(\lambda)$, obtained out of (7), by the active surface A_r will result in the spectral irradiance $E(\lambda)$ in W/m². The illumination E_v spatial distribution in the environment at the OPV height can be finally achieved by wavelength-weighing the spectral irradiance according to the luminous efficiency function [53] (see Fig. 14). The obtained illumination varies from 550 lx (in the corner of the room) up to 990 lx (in the centre), which is in accordance with the International Organization for Standardization, that defines the ideal illumination in workspaces between 300 lx and 1500 lx [63].

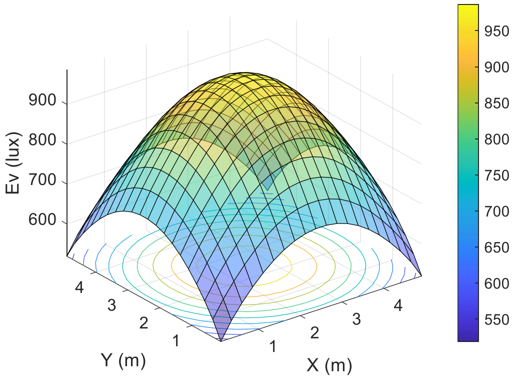

FIGURE 14. Illuminance level at the OPV height in the simulated room.

Similar to the illumination, the short-circuit current I_{sc} distribution can be obtained with post processing using the simulation result $h(t;\lambda)$ and (22). The lowest obtained current in this scenario is 150 μA, generated at the corners of the environment and associated to an illumination of 550 lx, rising up to 280 μA at the centre, associated to 990 lx. Analysing the diagonal axis of the room, starting from any corner, the short-circuit current I_{sc} extracted by the rectangular OPV can be compared with a hypothetical short-circuit current when the diffuse rays are not considered for the indoor scenario, i.e. only taking into account LOS contributions (see Fig. 15).

We can finally draw attention to the importance of considering the diffuse light in indoor scenarios. An increase of the short-circuit LOS current of approximately 95 μA is noticeable for each analysed position, representing an improvement of 172% at the corners and of 51% at the centre of the current scenario. In a limited access indoor IoT environment, the diffuse optical power represents a major

This article has been accepted for publication in IEEE Access. This is the author's version which has not been fully edited and content may change prior to final publication. Citation information: DOI 10.1109/ACCESS.2024.3378056

factor for system modelling and prediction, important for both ambient energy harvesting and VLC.

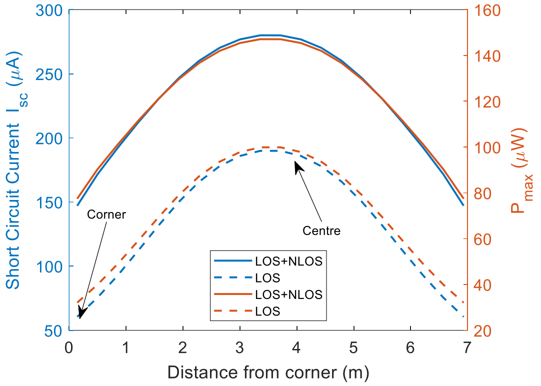

FIGURE 15. Simulated short-circuit current (in blue) and maximum output power (in red) generated by the OPV at the diagonal axis of the room when considering only LOS rays (dashed line) and LOS + NLOS rays (full line).

The I_{sc} can be further extended to energy harvesting performances by previous measurements of the OPV $I(V)$ and $P(V)$ curves at different light intensities (see Supp. Fig. 3 and Supp. Fig. 4, in supporting information). For each characterization, different parameters can be obtained, for instance the maximum output electrical power P_{max}, achieved at the MPP (see Supp. Fig. 5). The aforementioned static characterizations were realized under the same PSD than those used in the previous experiments in order to obtain precise power estimation. In a variable illumination going from 500 lux up to 1000 lux, the OPV cell provided a quasi-linear output power response from 78 μW to 150 μW. Using a smooth fitting function, the maximum output power, considering the OPV operating in the MPP, can be extrapolated for each simulated position from the obtained I_{sc} and E_v.

From the post processing results, we notice that the device can provide a minimum 77 μW at the corner, increasing up to 147 μW at the centre of the room (see Fig. 15). Extending the results to 300 lux, we estimate around 46 μW generated by the current OPV, resulting in a power density of 15.08 μW/cm². Contrastingly, in [43] (also for 300 lux), the PV panel attained a power density of 8.30 μW/cm² under identical illuminance conditions. Similarly, the OPV is expected to generate 10.05 μW/cm² under 200 lux, while in [45], the α-Si panel obtained 4.86 μW/cm² under the same illuminance. This underscores once more the remarkable performance OPVs for indoor IoT integration.

From the LOS rays, the maximum output power generated by the OPV cell can also be predicted when no diffuse channel is considered at the scenario (see Fig. 15). An underestimation of 50 μW is observed in all simulated positions, representing an increase of 185% at the corners and of 51% at the centre, which once more demonstrate the importance of diffuse light consideration for better system modelling in indoor IoT scenarios.

The simulation has shown the importance of OPV for indoor energy harvesting, which can generate decent power when positioned only 10 cm above the ground. Expanding the results for the IoT context, these power levels are interesting to supply different wireless nodes with variable communication protocols even at low illumination, such as a LoRA Backscatter (10 μW - 20 μW) and passive Wi-Fi (50 μW - 70 μW) [14], [64]. On the communication aspect, sending data trough light can be particularly effective for autonomous Light-based Internet-of-Things (LIoT) nodes while simultaneously harvesting ambient data [65].

Classical VLC configurations typically employ a TIA to convert the output current into a corresponding output voltage. In this setting, the solar cell operates either in photovoltaic mode (no bias voltage applied) or photoconductive mode (reverse bias voltage applied) [66]. In the first, the output current represents the device's short circuit current as its voltage is zero. By incorporating the actual short-circuit current I_{sc} along with noise analysis, the system signal-to-noise ratio (SNR) can be determined, facilitating the calculation of the theoretical maximum data rate with associated modulations.

Although the communication (channel data rate limitation) and energy harvesting (P_{max}) analysis were studied alone, the simulation of the OPV short-circuit current in IoT environments is in fact the first step for more complex simulations involving the receiver front-end adapted to the SLIPT concept. With the knowledge of the internal characteristics of the device, such as shunt or series resistances, appropriate equivalent and receiver circuits can be developed according to the communication/power requirements.

VII. CONCLUSION

In this work, we reviewed the wide-band optical propagation equations for general link scenarios (LOS + NLOS) while considering the relative responsivity $R_{rel}(\Psi)$ of the device. We also successfully demonstrated an optical channel MC simulation with a ray-tracing algorithm using a flexible, low-cost inkjet-printed OPV as receiver.

Our approach was based on an apprehensible connection between theory, simulation and experiment. Exploring the radiometric equations and simulation results, the channel impulse response and the OPV short-circuit current can be predicted for different optical link scenarios while accounting for its internal losses.

These preliminary simulation results, although realized in a simple cubic room, demonstrate the interest of optical channel simulations for complex indoor environments. In scenarios targeted for massive IoT nodes deployment, different surfaces induce non-directive paths, which plays an important role in the optical data/energy transmission. The simulation, paired up with the overwhelming indoor performance and flexibility of OPVs, illustrate the appeal of inkjet-printed organic electronics to supply low power connected devices. Thus, the analysis will be further evaluated for communication purposes by extending the static condition to the SLIPT context, taking into consideration different aspects that can influence the data transfer and energy harvesting performance.

Furthermore, this work invites future analysis on the front-end circuit simulation, emphasizing SLIPT context for IoT. The current work can also be fully extended to complex IoT scenarios simulations involving different obstacles and elements for both energy harvesting and data transfer. A simulator model of flexible receivers with experimental validation is also an interesting prospect that can be carried on from this work.

REFERENCES

[1] "Cisco Annual Internet Report - Cisco Annual Internet Report (2018–2023) White Paper," Cisco. Accessed: Jun. 20, 2023. [Online]. Available: https://www.cisco.com/c/en/us/solutions/collateral/executive-perspectives/annual-internet-report/white-paper-c11-741490.html

[2] M. Jatau, M. David, and S. Zubair, "LiFi: The Solution to Radio Frequency Saturation," in *2020 International Conference in Mathematics, Computer Engineering and Computer Science (ICMCECS)*, IEEE, Mar. 2020, pp. 1–6. doi: 10.1109/ICMCECS47690.2020.240880.

[3] H. Haas, L. Yin, Y. Wang, and C. Chen, "What is LiFi?," *Journal of Lightwave Technology*, vol. 34, no. 6, pp. 1533–1544, 2016, doi: 10.1109/JLT.2015.2510021.

[4] H. Haas, "Harald Haas: Wireless data from every light bulb | TED Talk." Accessed: Jun. 20, 2023. [Online]. Available: https://www.ted.com/talks/harald_haas_wireless_data_from_every_light_bulb

[5] M. Muller *et al.*, "LiFi with 5G for the Smart Factory," *IEEE Wireless Communications and Networking Conference, WCNC*, vol. 2022-April, pp. 2310–2315, 2022, doi: 10.1109/WCNC51071.2022.9771969.

[6] D. Ma, G. Lan, M. Hassan, W. Hu, and S. K. Das, "Sensing, Computing, and Communications for Energy Harvesting IoTs: A Survey," *IEEE Communications Surveys & Tutorials*, vol. 22, no. 2, pp. 1222–1250, 2020, doi: 10.1109/COMST.2019.2962526.

[7] Z. Ghassemlooy, W. Popoola, and S. Rajbhandari, *Optical Wireless Communications System and Channel Modelling with Matlab*. 2013.

[8] S. Fuada, A. P. Putra, Y. Aska, and T. Adiono, "Trans-impedance amplifier (HA) design for Visible Light Communication (VLC) using commercially available OP-AMP," in *2016 3rd International Conference on Information Technology, Computer, and Electrical Engineering (ICITACEE)*, IEEE, 2016, pp. 31–36. doi: 10.1109/ICITACEE.2016.7892405.

[9] T. Sanislav, G. D. Mois, S. Zeadally, and S. C. Folea, "Energy Harvesting Techniques for Internet of Things (IoT)," *IEEE Access*, vol. 9, pp. 39530–39549, 2021, doi: 10.1109/ACCESS.2021.3064066.

[10] S. Mohsen, "A Solar Energy Harvester for a Wireless Sensor System toward Environmental Monitoring," *Proceedings of Engineering and Technology Innovation*, vol. 21, pp. 10–19, Apr. 2022, doi: 10.46604/peti.2022.9210.

[11] M. M. Ferreira, M. P. M. G. Miguel, Z. F. Da Silva Filho, C. P. De Souza, Y. An, and O. Baiocchi, "Internet of Natural Things (IoNT): An Experimental Evaluation of Best Position to Harvest Thermal Energy from Trees," in *2023 IEEE International Conference on Smart Internet of Things (SmartIoT)*, Aug. 2023, pp. 196–202. doi: 10.1109/SmartIoT58732.2023.00035.

[12] Z. Albataineh, A. Andrawes, N. F. Abdullah, and R. Nordin, "Energy-Efficient beyond 5G Multiple Access Technique with Simultaneous Wireless Information and Power Transfer for the Factory of the Future," *Energies*, vol. 15, no. 16, Art. no. 16, Jan. 2022, doi: 10.3390/en15166059.

[13] S. Mohsen, A. Zekry, K. Youssef, and M. Abouelatta, "A Self-powered Wearable Wireless Sensor System Powered by a Hybrid Energy Harvester for Healthcare Applications," *Wireless Pers Commun*, vol. 116, no. 4, pp. 3143–3164, Feb. 2021, doi: 10.1007/s11277-020-07840-y.

[14] V. Pecunia, L. G. Occhipinti, and R. L. Z. Hoye, "Emerging Indoor Photovoltaic Technologies for Sustainable Internet of Things," *Advanced Energy Materials*, vol. 11, no. 29, 2021, doi: 10.1002/aenm.202100698.

[15] M. F. Müller, M. Freunek, and L. M. Reindl, "Maximum efficiencies of indoor photovoltaic devices," *IEEE Journal of Photovoltaics*, vol. 3, no. 1, pp. 59–64, 2013, doi: 10.1109/JPHOTOV.2012.2225023.

[16] T. C. Wu, Y. S. Long, S. T. Hsu, and E. Y. Wang, "Efficiency Rating of Various PV Technologies under Different Indoor Lighting Conditions," *Energy Procedia*, vol. 130, no. October, pp. 66–71, 2017, doi: 10.1016/j.egypro.2017.09.397.

[17] B. Li, B. Hou, and G. A. J. Amaratunga, "Indoor photovoltaics, The Next Big Trend in solution-processed solar cells," *InfoMat*, vol. 3, no. 5, pp. 445–459, 2020, doi: 10.1002/inf2.12180.

[18] H. Zheng *et al.*, "Emerging Organic/Hybrid Photovoltaic Cells for Indoor Applications: Recent Advances and Perspectives," *Solar RRL*, vol. 5, no. 7, pp. 1–17, 2021, doi: 10.1002/solr.202100042.

[19] R. Steim *et al.*, "Organic photovoltaics for low light applications," *Solar Energy Materials and Solar Cells*, vol. 95, no. 12, pp. 3256–3261, Dec. 2011, doi: 10.1016/j.solmat.2011.07.011.

[20] M. L. Parisi, S. Maranghi, L. Vesce, A. Sinicropi, A. Di Carlo, and R. Basosi, "Prospective life cycle assessment of third-generation photovoltaics at the pre-industrial scale: A long-term scenario approach," *Renewable and Sustainable Energy Reviews*, vol. 121, p. 109703, Apr. 2020, doi: 10.1016/j.rser.2020.109703.

[21] N. Shah *et al.*, "A Review of Third Generation Solar Cells," *Processes*, vol. 11, no. 6, Art. no. 6, Jun. 2023, doi: 10.3390/pr11061852.

[22] R. Arai, S. Furukawa, Y. Hidaka, H. Komiyama, and T. Yasuda, "High-Performance Organic Energy-Harvesting Devices and Modules for Self-Sustainable Power Generation under Ambient Indoor Lighting Environments," *ACS Applied Materials and Interfaces*, vol. 11, no. 9, pp. 9259–9264, Mar. 2019, doi: 10.1021/ACSAMI.9B00018/SUPPL_FILE/AM9B00018_SI_002.AVI.

[23] S. Hwang and T. Yasuda, "Indoor photovoltaic energy harvesting based on semiconducting π-conjugated polymers and oligomeric materials toward future IoT applications," *Polymer Journal 2022*, pp. 1–20, Nov. 2022, doi: 10.1038/s41428-022-00727-8.

[24] L. Xie *et al.*, "Recent progress of organic photovoltaics for indoor energy harvesting," *Nano Energy*, vol. 82, p. 105770, Apr. 2021, doi: 10.1016/j.nanoen.2021.105770.

[25] R. Suthar, H. Dahiya, S. Karak, and G. D. Sharma, "Indoor organic solar cells for low-power IoT devices: recent progress, challenges, and applications," *J. Mater. Chem. C*, vol. 11, no. 37, pp. 12486–12510, Sep. 2023, doi: 10.1039/D3TC02570E.

[26] M. Jahandar, S. Kim, and D. C. Lim, "Indoor Organic Photovoltaics for Self-Sustaining IoT Devices: Progress, Challenges and Practicalization," *ChemSusChem*, vol. 14, no. 17, pp. 3449–3474, 2021, doi: 10.1002/cssc.202100981.

[27] Z. Wang, D. Tsonev, S. Videv, and H. Haas, "On the Design of a Solar-Panel Receiver for Optical Wireless Communications with Simultaneous Energy Harvesting," *IEEE Journal on Selected Areas in Communications*, vol. 33, no. 8, pp. 1612–1623, 2015, doi: 10.1109/JSAC.2015.2391811.

[28] Z. Wang, D. Tsonev, S. Videv, and H. Haas, "Towards self-powered solar panel receiver for optical wireless communication," *2014 IEEE International Conference on Communications, ICC 2014*, pp. 3348–3353, 2014, doi: 10.1109/ICC.2014.6883838.

[29] W.-H. Shin, S.-H. Yang, D.-H. Kwon, and S.-K. Han, "Self-reverse-biased solar panel optical receiver for simultaneous visible light communication and energy harvesting," *Optics Express*, vol. 24, no. 22, p. A1300, 2016, doi: 10.1364/oe.24.0a1300.

[30] N. Lorriere *et al.*, "An OFDM testbed for LiFi performance characterization of photovoltaic modules," *2018 Global LIFI*

This article has been accepted for publication in IEEE Access. This is the author's version which has not been fully edited and content may change prior to final publication. Citation information: DOI 10.1109/ACCESS.2024.3378056

Congress, GLC 2018, vol. 2018-Janua, pp. 1–5, 2018, doi: 10.23919/GLC.2018.8319116.

[31] J. Fakidis, H. Helmers, and H. Haas, "Simultaneous Wireless Data and Power Transfer for a 1-Gb/s GaAs VCSEL and Photovoltaic Link," *IEEE Photonics Technology Letters*, vol. 32, no. 19, pp. 1277–1280, 2020, doi: 10.1109/LPT.2020.3018960.

[32] S. Das, E. Poves, J. Fakidis, A. Sparks, S. Videv, and H. Haas, "Towards Energy Neutral Wireless Communications: Photovoltaic Cells to Connect Remote Areas," *Energies 2019, Vol. 12, Page 3772*, vol. 12, no. 19, p. 3772, Oct. 2019, doi: 10.3390/EN12193772.

[33] S. Das, J. Fakidis, A. Sparks, E. Poves, S. Videv, and H. Haas, "Towards 100 Mb / s Optical Wireless Communications Using a Silicon Photovoltaic Receiver," *GLOBECOM 2020 - 2020 IEEE Global Communications Conference*, pp. 9–14, 2020, doi: 10.1109/GLOBECOM42002.2020.9322495.

[34] J. I. De Oliveira Filho, O. Alkhazragi, A. Trichili, B. S. Ooi, M. S. Alouini, and K. N. Salama, "Simultaneous Lightwave and Power Transfer for Internet of Things Devices," *Energies 2022, Vol. 15, Page 2814*, vol. 15, no. 8, p. 2814, Apr. 2022, doi: 10.3390/EN15082814.

[35] S. Sepehrvand, L. N. Theagarajan, and S. Hranilovic, "Rate-power trade-off in simultaneous lightwave information and power transfer systems," *IEEE Communications Letters*, vol. 25, no. 4, pp. 1249–1253, 2021, doi: 10.1109/LCOMM.2020.3047379.

[36] S. Kadirvelu *et al.*, "A Circuit for Simultaneous Reception of Data and Power Using a Solar Cell," *IEEE Transactions on Green Communications and Networking*, vol. 5, no. 4, pp. 2065–2075, Dec. 2021, doi: 10.1109/TGCN.2021.3087008.

[37] W. Lei, Z. Chen, Y. Xu, C. Jiang, J. Lin, and J. Fang, "Negatively Biased Solar Cell Optical Receiver for Underwater Wireless Optical Communication System With Low Peak Average Power Ratio," *IEEE Photonics Journal*, vol. 14, no. 4, Aug. 2022, doi: 10.1109/JPHOT.2022.3186702.

[38] M. Liu, S. Xia, M. Xiong, M. Xu, Q. Liu, and H. Deng, "NLOS Transmission Analysis for Mobile SLIPT Using Resonant Beam," *IEEE Transactions on Wireless Communications*, pp. 1–1, 2023, doi: 10.1109/TWC.2023.3277593.

[39] J. R. Barry, J. M. Kahn, W. J. Krause, E. A. Lee, and D. G. Messerschmitt, "Simulation of multipath impulse response for indoor wireless optical channels," *IEEE Journal on Selected Areas in Communications*, vol. 11, no. 3, pp. 367–379, Apr. 1993, doi: 10.1109/49.219552.

[40] A. Behlouli, P. Combeau, L. Aveneau, S. Sahuguede, and A. Julien-Vergonjanne, "Efficient Simulation of Optical Wireless Channel Application to WBANs with MISO Link," *Procedia Computer Science*, vol. 40, no. C, pp. 190–197, Jan. 2014, doi: 10.1016/J.PROCS.2014.12.027.

[41] A. Behlouli, P. Combeau, and L. Aveneau, "MCMC Methods for Realistic Indoor Wireless Optical Channels Simulation," *Journal of Lightwave Technology*, vol. 35, no. 9, pp. 1575–1587, May 2017, doi: 10.1109/JLT.2017.2662939.

[42] K. Lee, H. Park, and J. R. Barry, "Indoor Channel Characteristics for Visible Light Communications," *IEEE Communications Letters*, vol. 15, no. 2, pp. 217–219, Feb. 2011, doi: 10.1109/LCOMM.2011.010411.101945.

[43] C. S. Abella *et al.*, "Autonomous Energy-Efficient Wireless Sensor Network Platform for Home/Office Automation," *IEEE Sensors Journal*, vol. 19, no. 9, pp. 3501–3512, May 2019, doi: 10.1109/JSEN.2019.2892604.

[44] S. Zhang, N. Bristow, T. Wyn David, F. Elliott, J. O'Mahony, and J. Kettle, "Development of an organic photovoltaic energy harvesting system for wireless sensor networks; application to autonomous building information management systems and optimisation of OPV module sizes for future applications," *Solar Energy Materials and Solar Cells*, vol. 236, p. 111550, Mar. 2022, doi: 10.1016/J.SOLMAT.2021.111550.

[45] R. L. Rosa, L. Boulebnane, D. Croce, P. Livreri, and I. Tinnirello, "An Energy-Autonomous and Maintenance-Free Wireless Sensor Platform with LoRa Connectivity," in *2023 12th International Conference on Renewable Energy Research and Applications (ICRERA)*, Aug. 2023, pp. 461–464. doi: 10.1109/ICRERA59003.2023.10269437.

[46] M. L. Meli *et al.*, "Energy Autonomous Wireless Sensing Node Working at 5 Lux from a 4 cm2 Solar Cell," *Journal of Low Power Electronics and Applications 2023, Vol. 13, Page 12*, vol. 13, no. 1, p. 12, Feb. 2023, doi: 10.3390/JLPEA13010012.

[47] T. V. Tran and W.-Y. Chung, "High-Efficient Energy Harvester With Flexible Solar Panel for a Wearable Sensor Device," *IEEE Sensors Journal*, vol. 16, no. 24, pp. 9021–9028, Dec. 2016, doi: 10.1109/JSEN.2016.2616114.

[48] S. H. Lee, "A Passive Transponder for Visible Light Identification Using a Solar Cell," *IEEE Sensors Journal*, vol. 15, no. 10, pp. 5398–5403, 2015, doi: 10.1109/JSEN.2015.2440754.

[49] C. Carrascal, I. Demirkol, and J. Paradells, "On-demand sensor node wake-up using solar panels and visible light communication," *Sensors (Switzerland)*, vol. 16, no. 3, 2016, doi: 10.3390/s16030418.

[50] K. Hammoud, D. Schreurs, S. Pollin, and Z. Cui, "A Joint Opportunistic Energy Harvesting and Communication System Using VLC for Battery-Less PV-Equipped IoT," in *2023 IEEE International Conference on Communications Workshops (ICC Workshops)*, May 2023, pp. 1926–1931. doi: 10.1109/ICCWorkshops57953.2023.10283503.

[51] J. Bouclé, D. Ribeiro Dos Santos, and A. Julien-Vergonjanne, "Doing More with Ambient Light: Harvesting Indoor Energy and Data Using Emerging Solar Cells," *Solar 2023, Vol. 3, Pages 161-183*, vol. 3, no. 1, pp. 161–183, Mar. 2023, doi: 10.3390/SOLAR3010011.

[52] J. M. Kahn, "Wireless infrared communications," *Proceedings of the IEEE*, vol. 85, no. 2, pp. 265–298, 1997, doi: 10.1109/5.554222.

[53] K. Lee, "Indoor visible light communications with LED Lightings," 2011.

[54] P. H. Pathak, X. Feng, P. Hu, and P. Mohapatra, "Visible Light Communication , Networking , and Sensing : A Survey , Potential and Challenges," *IEEE Communications Surveys and Tutorials*, vol. 17, no. 4, pp. 2047–2077, Oct. 2015, doi: 10.1109/COMST.2015.2476474.

[55] J. Nelson, *The Physics of Solar Cells*. PUBLISHED BY IMPERIAL COLLEGE PRESS AND DISTRIBUTED BY WORLD SCIENTIFIC PUBLISHING CO., 2003. doi: 10.1142/p276.

[56] S. Bastiaens, W. Raes, N. Stevens, W. Joseph, and D. Plets, "New Photodiode Responsivity Model for RSS-based VLP," *2019 Global LIFI Congress, GLC 2019*, pp. 0–5, 2019, doi: 10.1109/GLC.2019.8864136.

[57] S. Bastiaens, W. Raes, N. Stevens, L. Martens, W. Joseph, and D. Plets, "Impact of a photodiode's angular characteristics on RSS-Based VLP accuracy," *IEEE Access*, vol. 8, pp. 83116–83130, 2020, doi: 10.1109/ACCESS.2020.2991298.

[58] J. L. Gardner and F. J. Wilkinson, "Angular effects in silicon photodiode responsivity comparisons," *Metrologia*, vol. 34, no. 2, pp. 111–114, 1997, doi: 10.1088/0026-1394/34/2/1.

[59] M. Pharr and G. Humphreys, *Physically Based Rendering: From Theory To Implementation*, vol. 2. 2004.

[60] F. J. López-Hernández, R. Pérez-Jiménez, and A. Santamaría, "Monte Carlo calculation of impulse response on diffuse IR wireless indoor channels," *Electronics Letters*, vol. 34, no. 12, pp. 1260–1262, Jun. 1998.

[61] A. Julien-Vergonjanne, S. Sahuguède, and L. Chevalier, "Optical Wireless Body Area Networks for Healthcare Applications," pp. 569–587, 2016, doi: 10.1007/978-3-319-30201-0_26.

[62] S. Joumessi-Demeffo, "Dispositif communicant par optique sans fil pour les transmissions audio à l'intérieur du cockpit d'un avion," PhD Thesis, Limoges, 2020.

[63] "ISO 8995 CIE S 008/E, International Standard for Lighting of indoor work places." 2002.

[64] I. Mathews, S. N. Kantareddy, T. Buonassisi, and I. M. Peters, "Technology and Market Perspective for Indoor Photovoltaic Cells," *Joule*, vol. 3, no. 6, pp. 1415–1426, Jun. 2019, doi: 10.1016/j.joule.2019.03.026.

[65] A. Perera and M. Katz, "Novel Data and Energy Networking for Energy Autonomous Light-based IoT Nodes in WPAN Networks," in *2023 IEEE Wireless Communications and Networking*

Conference (WCNC), Mar. 2023, pp. 1–6. doi: 10.1109/WCNC55385.2023.10119120.
[66] B. Black and G. Brisebois, "Transimpedance Amplifiers for Wide Range Photodiodes Have Challenging Requirements".

Daniel Ribeiro dos Santos received the electrical engineer diploma from Federal University of Paraíba (UFPB), João Pessoa, Brazil, in 2021. Since 2022, he is pursuing his Ph.D. degree in optoelectronics and optical wireless communications with the University of Limoges, France. His researches are developed within XLIM laboratory (UMR CNRS 7252, University of Limoges, France) and constitute organic photovoltaics indoor characterization, visible light communication and optical channel modelling.

Johann Bouclé is currently Associate Professor at XLIM Research Institute (CNRS UMR 7252, University of Limoges, France) and head of the "Printed Electronics for Telecoms and Energy" (ELITE) group. He obtained a PhD degree in Physics in 2004 (University of Le Mans, France) and was then appointed postdoctoral research associate in the United Kingdom, initially at Imperial College London and then at the University of Cambridge to develop novel hybrid solar cells based on polymers and metal oxide nanostructures from 2005 to 2007. Habilitated for Research Direction (HDR) since 2015, he started a new research axis at XLIM devoted to the application of organic and hybrid optoelectronic devices for optical wireless communications.

Anne Julien-Vergonjanne received the Ph.D. degree in microwave and optical communications from the University of Limoges, France, in 1987. She is Professor since 2006 with the National School of Engineers of Limoges (ENSIL-ENSCI) and develops research activities within the XLIM laboratory (UMR CNRS 7252, University of Limoges, France). She leads the SYCOMOR research team in the SRI axis (Systems and Intelligent Networks), around optical and radio communication systems and networks. Her current research activities are in the fields of optical wireless communication systems.

Sadok Ben Dkhil is currently the CTO of the French startup Dracula Technologies specialized in OPV by inkjet printing for indoor application. He obtained a PhD degree in Physics from Claude Bernard University, Lyon, France in 2012. After his PhD, he conducted his postdoctoral research on organic photovoltaic in France (CNRS, CINaM), England (Merck Group, Southampton) during 2012–2016 working on the optimization of the performance and stability of organic solar cells. His research focuses on the development of new indoor organic photovoltaic devices by inkjet printing technique.

Marie Parmentier is currently a development engineer at the French startup Dracula Technologies. She received her master's degree from Grenoble Alpes (UGA) University, Grenoble, France, in 2021. After that, she joined Dracula Technologies as a development engineer. The focus of her work is mainly on the development of stable ink formulation based on new organic semi-conducting materials for OPV.

Pierre Combeau received the B.S. and M.S. degrees in information processing: computer science, images, automatic, from the University of Poitiers, in 1999 and 2001, and the Ph.D. degree in electronics, optronics and systems from the University of Poitiers, in 2004. He is Habilitated for Research Direction (HDR) since 2022. Since 2005, he is an Associate Professor with the University Institute of Technology of Poitiers, and head of the Department of electrical engineering and industrial computing since 2022. He develops research activities within the XLIM Laboratory, in the Optical and Radio Communication System and Network Department, Poitiers University. He is the author of one book chapter, 23 articles in international journals and more than 60 conference papers. His research interests include the study of electromagnetic wave propagation for wireless communication systems in radio and optical frequency domains.

Stéphanie Sahuguède received the M.Sc. and M.Eng. degrees from the National School of Engineers of Limoges (ENSIL-ENSCI), University of Limoges, France, in 2006. She received the Ph.D. degree in high frequencies and optical telecommunications, University of Limoges, France, in 2009. She works currently as an Associate Professor with XLIM Laboratory (UMR CNRS 7252, University of Limoges, France) and ENSIL-ENSCI. She is a member of the SYCOMOR Team of the axis Smart System and Networks. Her research activities are oriented toward wireless body sensors networks, wireless optical communications and embedded system conception for applications in various IoT contexts such as smart health, smart home and smart city.